Ultrathin Twisted Stacked Gap-Plasmon Metasurface with Giant and Tunable Shortwave Infrared Chirality

Zexiang Han, Fei Wang, Juehan Sun, Xiaoli Wang,* and Zhiyong Tang

Ultrathin optical components with giant circular dichroism hold great promise for polarization-sensitive nanophotonics. However, existing chiral metamaterials often rely on complex-shaped nanoinclusions, and there remains a paucity of designs active in the shortwave infrared (SWIR) useful for telecommunication and night vision. Here a detailed numerical analysis of the chiroptical response of a simple twisted stacked variant of gap-plasmon metasurface is presented based on periodic nanohole arrays. Impressively, the 100-nm free-standing plasmonic metasurface can attain a thickness-normalized ellipticity of up to 74.2° μm^{-1} with tunable bands in the SWIR. Strong and robust optical activity is achieved through energy confinement by gap surface plasmons and effective inter-nanohole coupling, resulting in an intense superchiral near field. The ultrathin plasmonic metasurface serves as an excellent platform for refractive index sensing with a sensitivity S_n of up to 648.1 nm RIU^{-1} and field-enhanced enantiodiscrimination. The simple metasurface with strong SWIR chirality can enjoy a multitude of potential applications including polarization-sensitive photodetection, optical telecommunication, machine vision, medical imaging, and spectroscopy. These findings also offer insights into some fundamental design principles for twisted stacked aperture-based metasurfaces and should facilitate the development of new chiral metamaterials with exceptional performance.

1. Introduction

Flat optics continue to spark intense research interest as they have the potential to revolutionize traditional optical systems from smartphone cameras to light microscopes. To achieve a planarized profile, optical metasurfaces, which are quasi-2D arrays of artificial subwavelength structures, have been developed. The constituent building blocks, known as "meta-atoms," show exceptional designability, ranging from simple nanospheres,[1] nanorods,[2] split ring resonators,[3] and gammadions,[4] to plasmonic structures of complex morphologies—all of which act as optical antennae.[5] On the lateral dimension, because of inter-antenna coupling, metasurfaces display collective optical responses absent in the individual resonators, enabling their unique capability to modulate the properties of incoming electromagnetic waves. Along the vertical axis, they possess a planar profile with reduced thicknesses that are much smaller than the wavelength of the incident light with which they interact. For comparison, traditional optical components like waveplates typically rely on bulky materials that modulate the light propagation over significantly larger distances (in the millimeter or centimeter range) in the optical path, resulting in severe optical losses. This makes ultrathin metasurfaces excellent for use as energy-efficient, lightweight, and highly integrable optical devices with superior performance for beam splitting, optical encryption, holographic displays, image processing, and super-resolution imaging.[6–12]

Recently, chiral metasurfaces with the ability to discriminate between the different light polarization states are receiving increasing attention. In spite of the ubiquity of chirality in nature, the chiroptical effects of natural chiral substances such as proteins or sugars are inherently too weak to be utilized. Copious metasurface and metamaterials designs that demonstrate large optical activity, characterized by circular dichroism (CD), in the ultraviolet–visible regime (300–800 nm) were reported.[13–17] For instance, a gap-plasmon metasurface composed of asymmetrical gold split rings, silicon dioxide, and a gold underlay realized a maximum CD in reflection of about 0.99 at 635 nm.[18] In addition to traditional chiral metamaterials that incorporate symmetry-breaking elements, twisted stacked nanostructures also possess twist-induced geometrical chirality for polarization control as bi- or few-layer metasurfaces.[19] Xie et al. twist-aligned two anisotropic polydiacetylene thin films for a twisted bilayer metasurface.[20] The chiral film displayed a large transmissive CD signal up to 10°, corresponding to a thickness-normalized ellipticity of 35.3° μm^{-1}, at visible frequencies. Its tunable CD spectra further enabled multiplex full-color laser display and light polarization-based image encryption. Similar efforts on visible chiral metasurfaces have expanded the application portfolio to

Z. Han, F. Wang, J. Sun, X. Wang, Z. Tang
CAS Key Laboratory of Nanosystem and Hierarchical Fabrication
National Center for Nanoscience and Technology
Beijing 100190, P. R. China
E-mail: wangxl@nanoctr.cn
F. Wang, X. Wang, Z. Tang
Center of Materials Science and Optoelectronics Engineering
University of Chinese Academy of Sciences
Beijing 100049, P. R. China

**ADVANCED
SCIENCE NEWS**

www.advancedsciencenews.com

**ADVANCED
OPTICAL
MATERIALS**

www.advopticalmat.de

include anticounterfeiting measures,[21] visual alarms,[22] and holographic displays.[23]

Nevertheless, there is a shortage of chiral thin films and metasurfaces designed for operation in the shortwave infrared (SWIR).[24] Certain applications involving objects that obscure or block visible light benefit from the use of SWIR, such as quality control of products packaged in plastic bottles or remote sensing and geological exploration in cloudy, dusty territories. The SWIR also bears significance in other major technological areas. The near-infrared (NIR)-II and NIR-III wavelengths, covering the SWIR spectral band and making up what is known as the biological window, are desired targets for the emission wavelengths of fluorescent probes in bioimaging.[25] This is due to the minimal light scattering and absorption by water and blood, facilitating SWIR light to penetrate deeper into the tissue. The reduced autofluorescence compared to the visible region additionally allows for enhanced contrast for imaging-guided tumor resection and therapies.[26,27] Another example is fiber-optic telecommunication and future long-distance quantum networks, which place stringent requirements on the operation wavelength of light to be around 1500–1550 nm for which silica optical fiber losses are minimized.[28] Given the abundance of applications, many of which could greatly benefit from polarization selectivity, it is surprising that chiral nanostructures active in the SWIR regime are understudied compared to other frequency domains (e.g., ultraviolet–visible or terahertz). High-performance ultrathin SWIR metasurfaces remain relatively rare.

In this study, the SWIR chiroptical performance of a twisted stacked variant of gap-plasmon metasurface based on nanohole arrays is investigated by the finite element method. Plasmonic aperture arrays, one of the most fundamental structures in nanophotonics, with tailorable optical response from ultraviolet to the infrared serve as the basis of our design. In contrast with metamaterials that employ custom-designed nano-inclusions, where a single element would already have multiple parameters complicating the design space, our system represents a simpler alternative. Here, the 100-nm ultrathin plasmonic metasurface possesses a transmissive CD of >7°, corresponding to a design-specific optical chirality of up to 74.2° μm^{-1} at telecom wavelengths. Owing to tunable gap surface plasmon (GSP) modes, the CD peak wavelength is tunable from 1080 to 1510 nm in the SWIR with a large modulation depth accompanied by robust performance that is rarely seen in other systems. We further show that the plasmonic metasurface could be used for monitoring environmental index changes with high sensitivities. Moreover, the superchiral near-field generated by SWIR excitation onto the metasurface enables chiral sensing with enantiodiscrimination. This work presents a high-performance, ultrathin, SWIR chiral metasurface for a myriad of applications such as fiber-optical long-distance communication, night vision, and enantioselective biosensing.

2. Results and Discussion

2.1. Giant Circular Dichroism in Ultrathin Plasmonic Metasurfaces

The plasmonic metasurface is composed of two 25 nm thick gold films perforated with periodic circular nanoholes in a square array spaced by a 50 nm thick quartz interlayer (**Figure 1**). The ultrathin trilayer structure, with a thickness of only 100 nm, adopts a metal–insulator–metal (MIM) configuration in order to support near-field coupling between the metallic layers, accommodating GSP modes.[29,30] Its optical chirality originates from the chiral stacking of the periodic nanohole arrays, where the rotational alignment between the two array layers induces the breaking of geometric mirror symmetry for clockwise versus counterclockwise twisting directions. Figure 1a,c shows the two enantiomeric stacking configurations of the metasurface, where the left-handed (LH) design has the top layer twisted by 22.5° in the counterclockwise direction and the right-handed (RH) counterpart features a clockwise twist. The corresponding optical spectra under normally incident circularly polarized light are provided in Figure 1b,d and Figure S1 (see Supporting Information for details). The CD spectrum is calculated as the ellipticity angle given by

$$CD \; (deg) = \left(\frac{180°}{\pi} \right) \tan^{-1} \left(\frac{\sqrt{I_{RCP}} - \sqrt{I_{LCP}}}{\sqrt{I_{RCP}} + \sqrt{I_{LCP}}} \right) \qquad (1)$$

where $I_{RCP/LCP}$ is the intensity of the transmitted right circularly polarized (RCP) or left circularly polarized (LCP) light, respectively. Because the two twisted metastructures have opposite chiroptical signatures (Figure 1b,d), displaying helicity-dependent resonances, switching the direction of rotation could easily reverse the CD signal, analogous to other twisted stacked metasurfaces.[19] An untwisted nanohole-based MIM metastructure, on the other hand, is essentially chiroptically silent and allows most (≈75% on average) of the incoming SWIR waves to pass through (Figure S2, Supporting Information), demonstrating the typical extraordinary optical transmission behavior of aperture arrays.[31] For both twisted metasurfaces, two resonant features are identified. At the shorter wavelengths of 1200–1300 nm, the resonance bands that manifest as transmission dips occur at nonidentical wavelengths. For example, the optical response of the LH design has a transmission minimum at $\lambda = 1255$ nm for LCP excitation but at $\lambda = 1190$ nm for RCP excitation (Figure 1b). The disparate transmission minima positions under LCP and RCP light thus give rise to the Cotton effect in the bisignate CD signal centered around $\lambda = 1200$ nm, with the first CD resonance being positioned at $\lambda = 1275$ nm. The second resonant feature occurs at around 1510 nm for the LH metasurface, where the two transmission dips coincide in their spectral positions but possess different magnitudes in the intensity of the transmitted circularly polarized light. Analogous observations could be made for the RH design. Of note, the plasmonic metasurface could obtain a giant ellipticity magnitude of 7.15° and a Kuhn's dissymmetry factor of +0.48 at $\lambda \approx 1510$ nm, indicating an intrinsic high selectivity toward a certain polarization state of SWIR light depending on the handedness of the design. Because its thickness corresponds to merely 1/15 of its resonant wavelength, there is superior control over the optical wavefront of circularly polarized SWIR light within the ultrathin metastructure. The stacked MIM metasurface has a design-specific thickness-normalized ellipticity of 71.5° μm^{-1} in transmission, about four magnitudes higher than thin films of natural chiral sugars (≈10^{-2} deg μm^{-1}). The large figure of merit (FoM) stands among the highest values
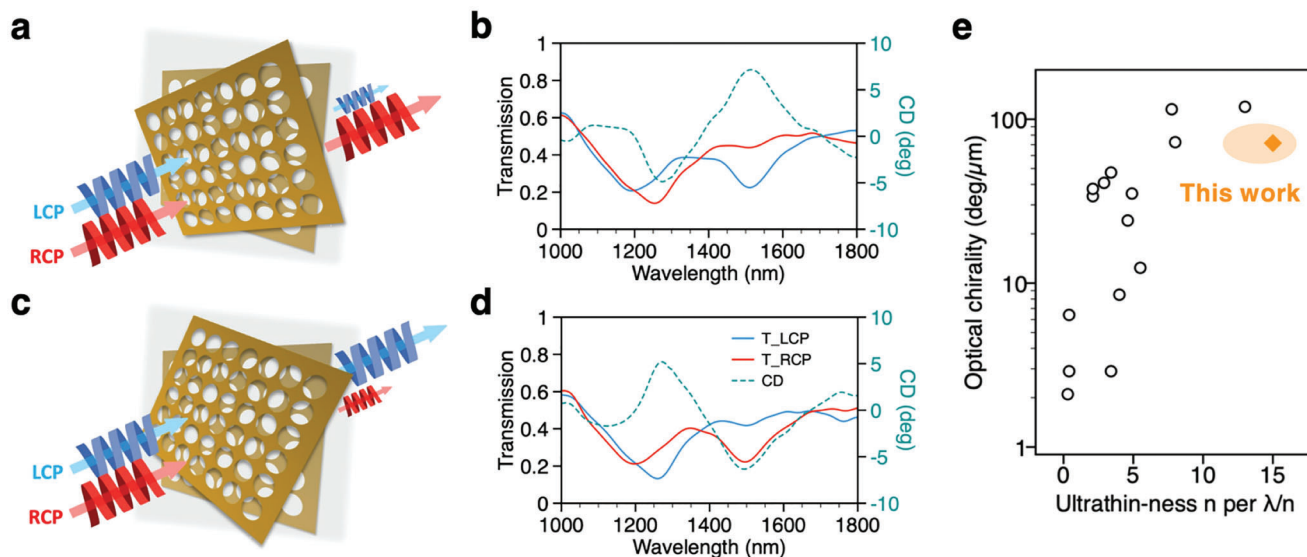
Figure 1. Optical response of the ultrathin chiral plasmonic metasurfaces. a) Schematic of the LH chiral metasurface. The design parameters are as follows: thickness of the nanohole arrays $t = 25$ nm, nanohole diameter $D = 780$ nm, lattice periodicity $P = 800$ nm, interlayer spacing $h = 50$ nm, and twist angle $\theta = 22.5°$. b) Calculated transmission and CD spectra for the LH metasurface. c,d) Schematic of the RH-twisted chiral metasurface and its calculated transmission and CD spectra. e) Comparison of the FoM of state-of-the-art transmissive chiral thin films and metamaterials operating in the SWIR. The ultrathinness is quantified by n, which is the inverse value of the fraction of the material's thickness with respect to its CD resonant position. See Table S1 (Supporting Information) for details.

ever-reported for chiral metamaterials that function in the NIR/SWIR (Figure 1e).[32–45]

We acknowledge that the present study focuses on the chiroptical behavior of the twisted stacked metasurface at normal incidence. However, it is important to take note of the dependence of the chiral response of our nanohole-based design on the illumination angle, as the diffractive excitation nature of the surface plasmon polaritons in the aperture array becomes apparent when obliquely illuminated.[46] Specifically, an enhanced CD performance of our metasurface could be expected at non-normal incidence, as evidenced by previous reports.[46–48] The CD maximum is likely positioned at a different wavelength due to the extrinsic chiral resonance at play, yet investigating that these aspects fall beyond the scope of this work. In the following sections, detailed analyses on the metasurface's chiroptical response to normally incident polarized light will be presented.

2.2. Near-Field Origin of the Optical Chirality

We carry out near-field analysis based on full-wave electromagnetic simulations to elucidate the origin of the strong chiroptical response of the LH metasurface. **Figure 2**a,b displays the surface charge maps across the entire supercell of the metasurface at three wavelengths of interest; namely, $\lambda = 1190$, 1255, and 1510 nm to help clarify gap-plasmon excitation. A number of dipole and multipole textures are observed in the array layers. Despite its complexity, key messages could be deduced by examining the propagation directions of surface currents flowing from positive to negative charges. To start, when the incident light impinges on the top Au nanohole array, surface currents are

induced, which predominantly travel along a given lattice direction as illustratively indicated by the white arrows (Figure 2a,b). Further examination of the surface current vector fields corroborates this observation (Figures S3 and S4, Supporting Information). However, as light propagates and arrives at the bottom Au layer, there is no longer a prevailing co-propagation of electron currents within the array structure, contrary to previously reported.[49] Instead, some charge monopole-like features with diverse multipole textures appear at the top surface of the bottom array layer. For example, helical-like surface currents are induced at various positions of the supercell in the bottom Au layer under RCP irradiation. The observation of multipole surface plasmons points to the strong coupling between adjacent nanoholes for sufficiently large apertures.[50] The dipoles, and multipoles alike, across the two twisted Au layers could couple to form plasmonic modes with field confinement evidenced by the localization of the intense electric and magnetic fields in the dielectric region of the MIM metastructure (Figures S5 and S6, Supporting Information), i.e., indicating the formation of internal surface plasmon polaritons or gap surface plasmons. The substantial disparities between the charge distribution features in the bottom layer, and thus across the MIM metasurface, at $\lambda = 1190$ and 1225 nm signal significant differences in the interarray layer coupling at the two wavelengths under polarized incidences. Together with the different intensities of the transmitted LCP and RCP waves at the two wavelengths seen in their respective field distributions (Figure S5, Supporting Information), this gives rise to the Cotton effect with a bisignate CD signal at around 1200 nm.

For the second resonant feature at $\lambda = 1510$ nm, the surface currents are overall traversing in opposing lattice directions in the top Au layer under LCP versus RCP light (Figure S7,
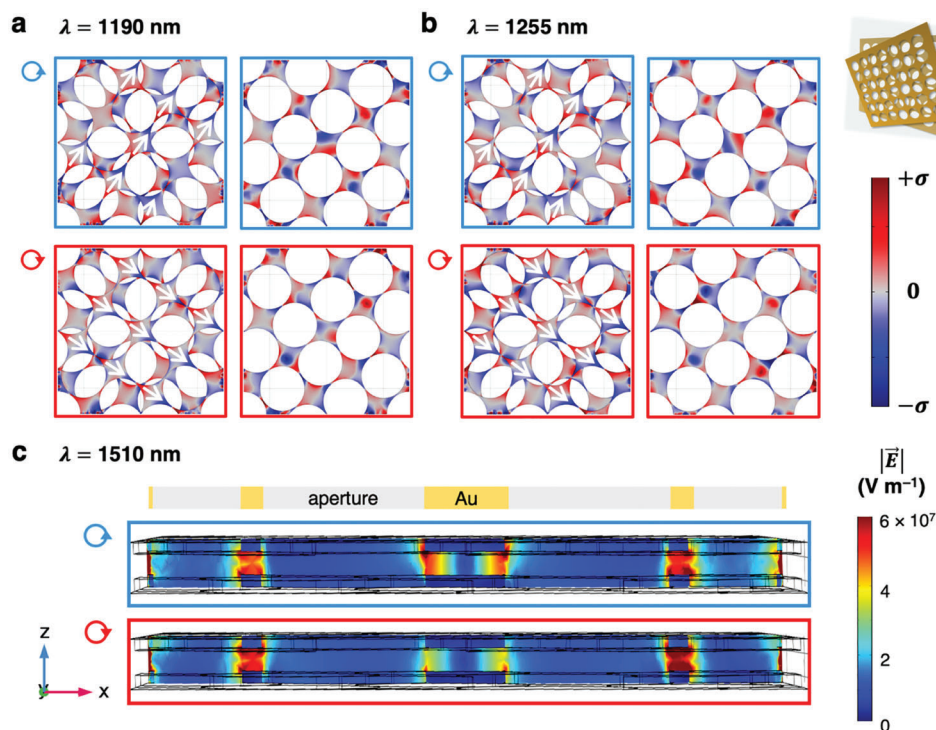
ADVANCED
SCIENCE NEWS

www.advancedsciencenews.com

ADVANCED
OPTICAL
MATERIALS

www.advopticalmat.de

Figure 2. Near-field analysis of the LH plasmonic chiral metasurface. a,b) Top view of the normalized surface charge distribution of the metasurface supercell and the bottom Au layer, respectively, illuminated by LCP and RCP light at a) $\lambda = 1190$ nm and b) $\lambda = 1255$ nm. Arrows indicating surface current propagation directions are shown for illustrative purposes. c) Cross-sectional view of the electric field distribution in the metasurface under 1510 nm LCP and RCP light (not to scale). The viewing plane is the xz-plane along the central axis of the metasurface supercell.

Supporting Information). Although the surface charge maps appear distinct for the two polarization states, the spatial distributions of the bonding (from counterpropagating currents) and antibonding coupling (from copropagating currents) between the Au layers are highly similar as illustrated in Figure S7 (see relevant discussions in the Supporting Information). This accounts for the identical resonant spectral positions for the transmission dips under LCP and RCP light. Besides that, unlike at the shorter wavelengths, the surface charge distribution shows mostly dipole-like textures for both LCP and RCP incidences, suggesting a resonance mode different from before at this wavelength. As is expected for an MIM superstructure, the electric field becomes concentrated in the insulating SiO_2 spacer between the two Au layers, creating numerous plasmonic hotspots and clearly supporting the gap plasmons in the interlayer (Figure 2c). The existence of magnetic hotspots with significant magnetic resonance effects could too be seen (Figure S8, Supporting Information). In particular, the spatial distributions of both the electric and magnetic fields within the LH metasurface when subject to LCP and RCP irradiations show qualitative resemblance, respectively, observing only a reduction in the averaged field intensity for each under RCP light (Figures S8 and S9, Supporting Information). This signals a difference in the excitation strength and magnetic resonance that manifests as a difference in the transmittance of 1255 nm polarized light as shown in Figure 1b, which in conjunction with the same mode excitation leads to a large ellipticity of +7.15° at this wavelength.

We further quantify the local density of chiral asymmetry of the electromagnetic field in the ultrathin plasmonic metasurface by calculating the superchiral field via[51]

$$C = -\frac{\omega \varepsilon_0}{2} \mathfrak{I} \left(\vec{E}^* \cdot \vec{H} \right) \qquad (2)$$

where ω is the angular frequency, ϵ_0 is the free-space permittivity, $\mathfrak{I}$ denotes the imaginary part, the asterisk denotes the complex conjugate of a field, and $\vec{E}$ and $\vec{H}$ are the electric and magnetic fields, respectively. **Figure 3**a shows the superchiral field evolution across the metasurface at 1510 nm where the LH metasurface obtains its highest polarization selectivity toward LCP light. As LCP SWIR light first impinges onto the metasurface, there is minimal cross-coupling between the electric and magnetic components at the air/Au interface as evidenced by the near-zero local chiral asymmetry. Then, the superchiral field becomes confined into nanoscale volumes in the interlayer region that is sandwiched between the two rotationally aligned plasmonic aperture arrays, with negligible superchirality at the exiting face of the metasurface. This makes physical sense give the significant field enhancement via simultaneous electric and magnetic resonances across the MIM structure. Similar superchiral field confinement is seen for the LH metasurface under RCP irradiation (Figure 3b), though to a markedly reduced extent due to the left-handedness of the design with strong LCP absorption. The results demonstrate the exception control over the local chiral asymmetry within the 100 nm planar profile.
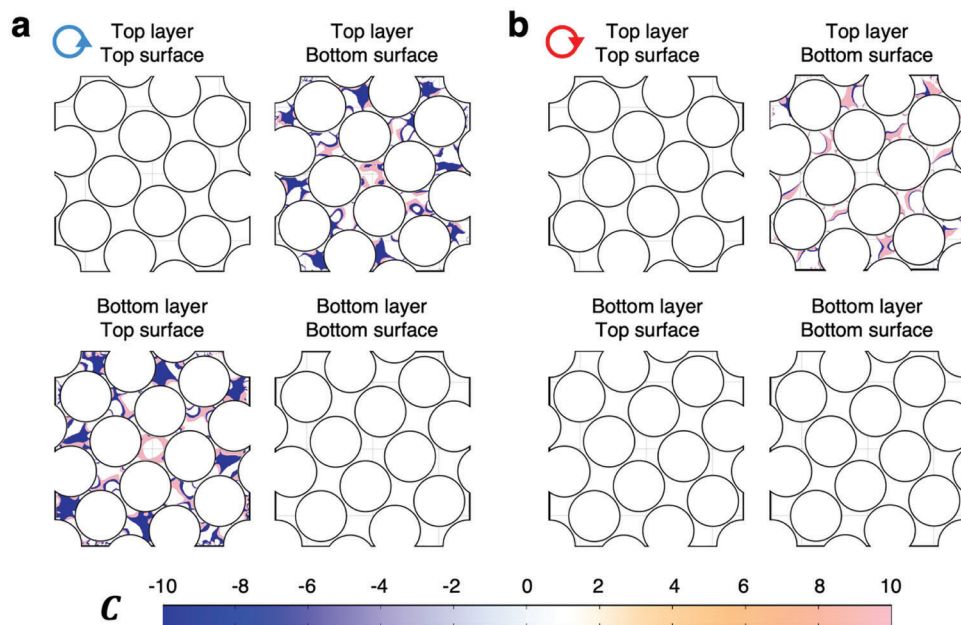
**ADVANCED
SCIENCE NEWS**

www.advancedsciencenews.com

**ADVANCED
OPTICAL
MATERIALS**

www.advopticalmat.de

Figure 3. Superchiral field evolution across the LH chiral metasurface under a) LCP and b) RCP light at 1510 nm. The four interfaces of interest are selected to be the air/Au_{top} interface, Au_{top}/dielectric interface, dielectric/Au_{bottom} interface, and finally Au_{bottom}/air interface.
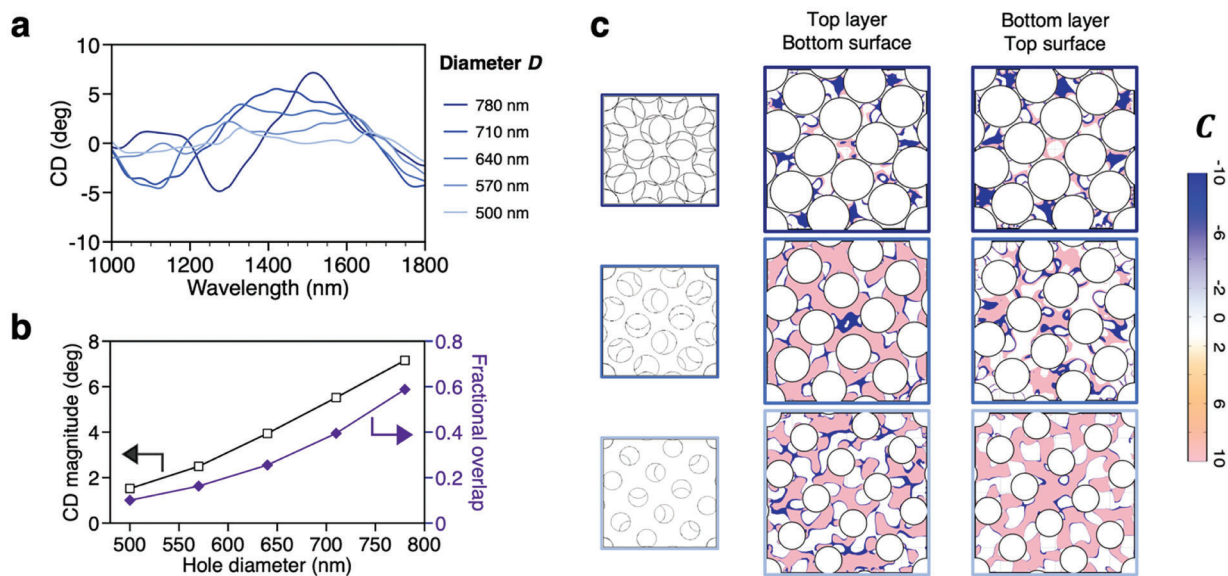

Figure 4. Substantial nanohole overlap is necessary to generate a large chiral response via strong interantenna coupling. a) CD spectra of chiral metasurfaces with different hole diameters D. Other design parameters remain fixed as follows: $t = 25$ nm, $P = 800$ nm, $h = 50$ nm, and $\theta = 22.5°$. b) Effects of nanohole size on the CD maxima and its correlation with the fractional overlap of nanoholes. c) Superchiral field distributions at the two Au/dielectric interfaces of the three metasurfaces under LCP irradiation, with $D = 780$, 640, and 500 nm, respectively.

2.3. Importance of Interantenna Coupling in Twisted Stacked Metasurfaces

The optical properties of metamaterials and metasurfaces are largely determined by the constituent elements and their interactions. For arrays of subwavelength apertures, the holes are considered inverse antennae capable of controlling the profile of incident electromagnetic waves.[52,53] How the interelement coupling affects the chiroptical performance of a twisted stacked metasurface is yet to be explored systematically. We investigate this in our chiral metasurface by changing the nanohole size in an identical MIM metastructure with the same array periodicity. As the nanohole diameter decreases, the aperture-only region in the 2D projection image of the twisted metastructure is reduced (see inset schemes in **Figure 4**). Decreasing the nanohole diameter D leads to continuously diminished CD signals in the positive

**ADVANCED
SCIENCE NEWS**

www.advancedsciencenews.com

**ADVANCED
OPTICAL
MATERIALS**

www.advopticalmat.de

resonant band in the range λ = 1400–1600 nm (Figure 4a). For example, the maximum CD signal drops to only 21% of its original value when reducing the nanohole size from 780 to 500 nm. Additional modes become apparent as D decreases, which could be explained by the dependence of the optical resonance energy on hole diameter,[54] leading to the concurrent broadening of the CD band. These new excitation modes could be similarly inferred from the absorption and reflection spectra given in Figure S10 (Supporting Information). Figure S10 (Supporting Information) also illustrates how, as D is reduced to 500 nm where there is merely 10% of aperture-only region in the supercell, the plasmonic metasurface behaves more like a reflective metallic film. The significantly reduced transmission for both LCP and RCP light would in part explain the substantial reduction in the overall CD magnitude. For the sake of analysis, we define a phenomenological parameter, the fractional overlap of nanoholes, to be the fraction of the aperture-only region with respect to its maximum—that is, an untwisted bilayer would have a fractional overlap of 100%. Interestingly, a positive correlation between the fractional overlap of the nanoholes in the twisted stacked metasurface and its CD performance is found (Figure 4b). This observation could be leveraged to rationalize previous findings on Moiré metamaterial composed of smaller nanoholes in a hexagonal array,[49] where changing the rotation angles of the twisted metamaterial has a minimal influence on the magnitude of the CD response. We attribute this to the relative twist-independent spatial overlap of the nanoholes ($\approx$0.24 according to our reanalysis of previous data[49]) in the direction of incident light.

It is reasonably hypothesized that the reduced fractional overlap of nanoholes in the twisted stacked metasurface leads to diminished hole–hole coupling and thus the chiroptical performance. To validate this, superchiral fields at the Au_{top}/dielectric interfaces are examined for three metasurfaces with D = 780, 640, and 500 nm (Figure 4c). Our analysis focuses on the near-field behavior at the wavelengths where each metasurface exhibits maximum CD, that is, λ = 1510, 1330, and 1330 nm. When the LH chiral metasurface has the largest nanohole diameter of 780 nm, negative-valued optical superchirality C dominates at the interface, indicative of the strong coupling of the metasurface to LCP light. As the nanohole size decreases, the areal fraction of such negative-valued chiral field asymmetry becomes diminished, pointing to the reduced chiral light–matter coupling that contributes to the positive CD. This makes sense because of the reduced physical proximity of the hole edges that act as resonators for smaller aperture sizes. Therefore, when the nanohole is sufficiently large in a given sized unit cell, not only is there strong inter-nanohole coupling in individual array layers accompanied by multipole textures in plasmon excitation,[50] but there also exists enhanced inter-nanohole coupling across the metastructure. The results in Figure 4 demonstrate that the nanohole spatial overlap could act as a physical ruler to gauge the extent of interantenna coupling and the effectiveness of chiral light–matter interactions in our twisted stacked MIM metasurface.

2.4. Tunable and Robust Near-Infrared CD Response

The extensive near-field analysis above confirms the existence of GSP modes supported by our chiral plasmonic metasurface. The
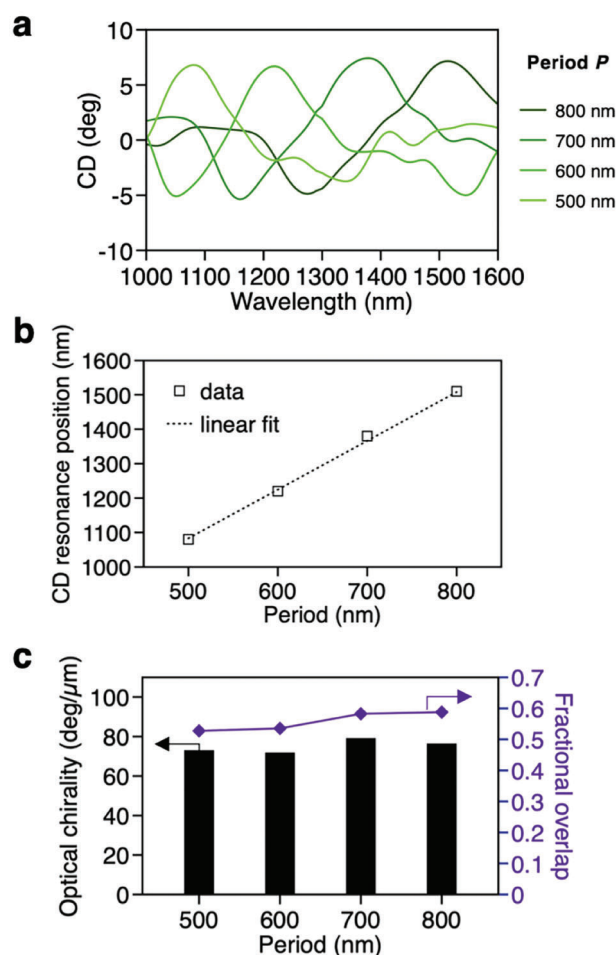

Figure 5. Tunable operation wavelengths of the chiral plasmonic metasurface in the NIR/SWIR. a) CD spectra for LH chiral metasurfaces with different lattice periodicities P. The nanohole sizes are chosen such that P = D + 20 nm. b) The spectral position of the positive CD band as a function of lattice periodicity. c) Comparison of the FoM, thickness-normalized ellipticity, and the spatial overlap of nanoholes for the corresponding chiral metasurfaces.

GSP mode is known to be tailorable. For stacked nanohole arrays in an MIM configuration, its resonant wavelength λ_{GSP} obeys the functional relationship[31]

$$\lambda_{GSP} = \frac{P\sqrt{\epsilon_s}}{\sqrt{\frac{h}{h + \frac{\lambda_p \coth(k_p t)}{\pi}}}} \qquad (3)$$

where P is the lattice periodicity, ϵ_s is the dielectric function of the dielectric spacer layer, h is the dielectric spacer thickness, λ_p is the plasma wavelength of the metal with $k_p = \frac{2\pi}{\lambda_p}$, and t is the thickness of the metal layer. This thus warrants tunability of the spectral response in the metasurface by simply changing the lattice periodicity P while ensuring a sufficiently large unit-cell nanohole size (**Figure 5**a). Specifically, Figure 5b shows that decreasing the lattice period shifts the CD resonance position toward shorter wavelengths, with an adjustable
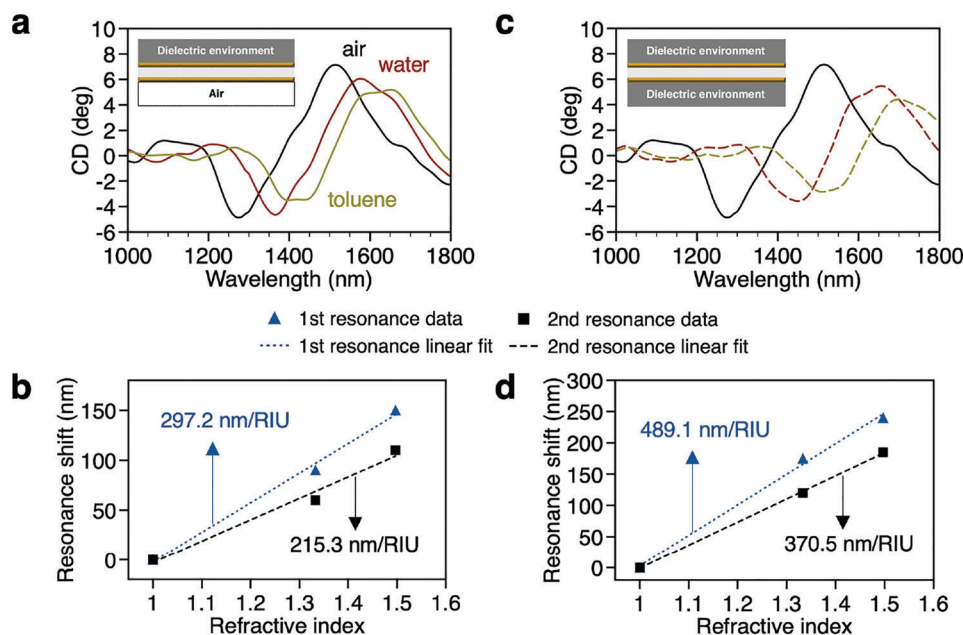
**ADVANCED
SCIENCE NEWS**

www.advancedsciencenews.com

**ADVANCED
OPTICAL
MATERIALS**

www.advopticalmat.de

Figure 6. Refractometric sensing using the chiral plasmonic metasurface. a) CD spectra of the LH metasurface with different environments on one side of the metasurface. b) CD resonance shifts versus refractive index of the medium on one side of the metasurface. c,d) Corresponding CD spectra and calibration curve for the sensing configuration where there is dielectric change on both sides of the metasurface. The refractive indices of air, water, and toluene are 1.000, 1.333, 1.497, respectively.

range from 1080 to 1510 nm, and there is a strong, positive linear correlation between λ_{GSP} and P in agreement with the analytical expression per Equation (3). The modulation depth, defined as $\frac{\lambda_{high} - \lambda_{low}}{\lambda_{low}} \times 100\%$, is 39.8%. Noteworthily, the magnitude of the CD signal, and consequently the FoM thickness-normalized ellipticity, remains consistently high for the spectral tuning strategy illustrated (Figure 5c; Table S1, Supporting Information). Two key factors contribute to the strong CD performance. First, the polarization-resolved transmission spectra of the plasmonic metasurfaces display the same two distinct resonance features as detailed earlier, pointing to an identical chiroptical origin in the twisted metasurfaces with different lattice periods (Figure S11, Supporting Information). Second, the spatial overlap of nanoholes, a key determinant of inter-nanohole coupling, is similarly high for the four metasurfaces, accounting for the comparable giant ellipticities. The ultrathin chiral metasurface presented here is therefore superior to the majority of the metamaterial designs seen in the literature, which either possess limited tunability or are tunable yet with appreciable compromises in their chiroptical performance—such as via electric field application or physical actuation in Kirigami metasurfaces. On the other end of the spectrum, the much-less-reported tunable chiral metamaterials with robust performance and a large modulation depth (examples include ref.[55]) would typically necessitate simultaneous changes of the multiple unit cell parameters in order to achieve the same level of performance, whereas the need for such procedural optimization search is eliminated for our simple aperture array design. As the design engineering only deals with dimensions in intervals of 100 nm, nanofabrication requirements are significantly relaxed as well. To sum up, the tailorable GSP modes in our twisted stacked chiral metasur-

face allow us to program its CD spectral response in a straightforward and predictable manner, accompanied by a large modulation depth while retaining its robust optical activities.

2.5. Chiral Metasurface for Refractive Index Sensing

In plasmonic refractometric analysis, an increase in the bulk dielectric refractive index causes a corresponding decrease (or increase) in the plasmonic mode frequency (or wavelength). Yet this is hardly exemplified for SWIR metamaterials despite the known use of SWIR for inspection science including liquid analysis. We explore the use of the freely suspended SWIR plasmonic metasurface for index sensing under two configurations: i) dielectric environment change on one side of the metasurface, and ii) dielectric change on both sides of the metasurface. **Figure 6**a,c shows the calculated CD spectra of the LH metasurface in air ($n = 1$), water ($n = 1.333$), and toluene ($n = 1.497$) for the two sensing configurations. Both cases illustrate how an increment in the local index of refraction of the dielectric environment shifts the CD resonances toward longer wavelengths while observing a concurrent reduction in the CD magnitude. When one side of the dielectric medium is changed from air to other liquids, i.e., the neighboring environment being antisymmetric in nature, the sensitivity $S_n = \frac{\Delta\lambda}{\Delta n}$, where $\Delta\lambda$ is the resonance shift in the CD signal and Δn being the change in refractive index, is determined as the slope of the calibration curve to be 297.2 nm RIU^{-1} for the first CD resonance and 215.3 nm RIU^{-1} for the second resonance (Figure 6b). When both sides are immersed in the same medium, the chiral metasurface realizes a higher spectral sensitivity S_n of 489.1 nm RIU^{-1} for the lower-wavelength resonance mode, whereas monitoring the

**ADVANCED
SCIENCE NEWS**

www.advancedsciencenews.com

**ADVANCED
OPTICAL
MATERIALS**

www.advopticalmat.de

higher-wavelength resonance mode leads to an S_n of 370.5 nm RIU^{-1} (Figure 6d). The relatively enhanced detection sensitivity for a symmetric dielectric environment was similarly observed by others.[56] Because these environment-induced resonance shifts also occur in the transmission characteristics of the plasmonic metasurfaces (Figure S12, Supporting Information), we further inspect the behavior of transmission dips under linearly polarized light for potential index sensing. Interestingly, even though the spectral shifts show similar trends, the calculated S_n values are smaller compared to those when monitoring CD resonances for the case of antisymmetric dielectric media (Figure S13, Supporting Information). On the other hand, monitoring the transmittance of linearly polarized SWIR could enable the highest index sensitivity S_n of 648.1 nm RIU^{-1}, partly owing to the hybridization of the two resonances that yields larger spectral shifts. Based on these metrics, our ultrathin metasurface is on par with traditional nanohole arrays[57] and outperforms some recently reported SWIR metasurfaces.[36,58] The plasmonic metasurface could therefore discriminate refractive index changes in its local environment in a highly sensitive fashion, especially as a freestanding film with both sides being exposed to the same targeted liquid/medium.

2.6. Chiral Metasurface for Chirality Sensing and Enantiodiscrimination

The ability to produce superchiral optical near fields represents a hallmark of chiral metamaterials. One application that takes advantage of this enhanced chiral light–matter coupling is to detect chiral molecules of different handedness and differentiation thereof, which is of practical importance in biology, pharmaceutical science, and pesticide science. Here, an artificial chiral medium is considered similar to earlier works[59,60] (see the "Experimental Section" for details), and we apply the polarization-sensitive metasurface to detect and discriminate between chiral thin films termed "chiral$_+$" and "chiral$_-$" in the interlayer region, which as previously demonstrated possesses electric and magnetic hotspots with significant resonance effects and strong cross-coupling. The zoomed-in views of the CD responses with chiral analytes and/or racemates are shown in **Figure 7**. Depending on the handedness of the analyte, small spectral shifts are observed for the CD resonance around $\lambda \approx 1540$ nm for both LH and RH designs. Specifically, in the presence of chiral$_+$, the CD resonance of the metasurface–analyte composite redshifts slightly with respect to the racemate because of a larger effective refractive index, whereas it blueshifts for the chiral$_-$ enantiomer. To isolate the field-enhanced spectral signals, we remove the background signal from the plasmonic metasurface by calculating the enantiomer-induced CD spectral changes

$$\Delta CD_{\pm} = \left(CD_{RH\pm} - CD_{RH,racemic} \right) + \left(CD_{LH\pm} - CD_{LH,racemic} \right) \quad (4)$$

where $CD_{RH/LH}$ is the CD spectrum of the RH- or LH-metasurface in the presence of a 50 nm layer of chiral$_+$ (or chiral$_-$) medium, and racemic indicates the alternative presence of the racemic mixture. Figure 7c shows that the induced ΔCD spectra are mostly positive for chiral$_-$ and mostly negative for chiral$_+$ around the CD resonance, demonstrating the capability of the chiral
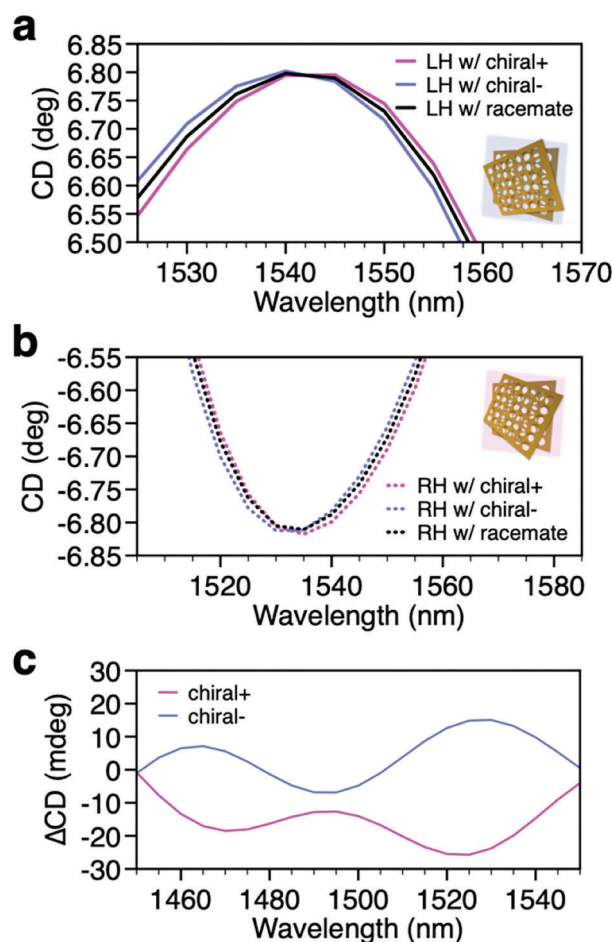

Figure 7. Label-free chirality sensing and enantiodiscrimination. a) Selected-area CD spectra for the LH metasurface with a 50 nm thin film of the chiral medium or its racemic mixture in the interlayer. b) Corresponding CD spectra for the RH metasurface. c) Calculated analyte-induced ΔCD upon background removal per Equation (4).

metasurface for enantiodiscrimination. It is worth noting that, in the absence of the plasmonic metasurface, the CD signal of this specific chiral medium would be zero because of nought absorption/extinction in the SWIR. Yet the ΔCD spectra display nonzero readings, hinting at the considerable coupling between the chiral metasurface and small molecule owing to the strong field confinement with optical superchirality that enables their sensitive detection.

3. Conclusion

This work presents a simple, ultracompact, chiral plasmonic metasurface design by means of twisted stacking for SWIR flat optics. With a mere thickness of 100 nm, the twisted gap-plasmon metasurface displays robust, giant transmissive CD responses and a remarkable thickness-normalized ellipticity of up to 74.2° μm^{-1}, which ranks among the highest values reported for nano/metastructures in the NIR/SWIR. Several design principles for twisted stacked aperture-based metamaterials are highlighted. First, chirality signal reversal is easily achieved by

**ADVANCED
SCIENCE NEWS**

www.advancedsciencenews.com

**ADVANCED
OPTICAL
MATERIALS**

www.advopticalmat.de

switching the twisted stacking configuration. Second, maximal spatial overlap of nanohole antennae in the direction of light incidence, which mediates strong interantenna coupling via simultaneous electric and magnetic resonances across the MIM metastructure, is key to maximizing the CD performance. Third, the tunability of GSP modes in the gap-plasmon metasurface allows for the precise control of the operation wavelengths from 1080 to 1510 nm, realizing a significant modulation depth accompanied by a consistent and ultrahigh performance. We further quantitatively demonstrate the use of the planar metasurface for refractive index sensing (with a spectral sensitivity S_n of up to 648.1 nm RIU^{-1}) and enantiodiscrimination of chiral analytes. Overall, the proposed chiral plasmonic metasurface has excellent chiroptical performance and could serve as a strong candidate for a suite of polarization-selective SWIR applications beyond the dual-mode sensing presented here. Its ultrathinness should also enable easy on-chip integration and is an attractive feature for miniaturized nanophotonic devices.

4. Experimental Section

System Setup: Finite-element calculations of the optical spectra and field distributions of the chiral plasmonic metasurfaces were carried out using the commercial software COMSOL Multiphysics.[61] In this work, the free-standing metasurface was composed of two planar periodic gold nanohole arrays rotationally aligned at an angle and separated by a dielectric interlayer. The design parameters are as follows: thickness of the nanohole arrays t, nanohole diameter D, lattice periodicity P, interlayer spacing h, and the twist angle θ. The interlayer spacer of choice was SiO$_2$, and the nanoholes were filled with the same medium. Frequency-dependent optical constants of gold were adopted from Johnson and Christy,[62] and those of SiO$_2$ were cited from the materials library of COMSOL.

Calculation of Optical Spectra: Absorbance was calculated as $A = 1 - T - R$, where T and R are the transmittance and reflectance as defined by the power ratios $T = \frac{P_{transmitted}}{P_{incident}}$ and $R = \frac{P_{reflected}}{P_{incident}}$. The calculated spectra had a spectral resolution of 5 nm per step, and all the spectra were smoothed out using a fast Fourier transform (FFT) filter with a smoothing factor of 5. To demonstrate chirality sensing, artificial optical constants relevant for realistic chiral media were used in the CD spectral calculations in the SWIR. The optical constants of the enantiomers are given by $\bar{n}_\pm = \bar{n}_{achiral/racemic} \pm \kappa$, where κ is the Pasteur parameter which takes the value of 10^{-3} for simulation purposes.

Supporting Information

Supporting Information is available from the Wiley Online Library or from the author.

Acknowledgements

Conflict of Interest

The authors declare no conflict of interest.

Data Availability Statement

The data that support the findings of this study are available from the corresponding author upon reasonable request.

[1] F. A. A. Nugroho, P. Bai, I. Darmadi, G. W. Castellanos, J. Fritzsche, C. Langhammer, J. Gómez Rivas, A. Baldi, *Nat. Commun.* **2022**, *13*, 5737.
[2] G. Vecchi, V. Giannini, J. G. Rivas, *Phys. Rev. Lett.* **2009**, *102*, 146807.
[3] N. Liu, H. Liu, S. Zhu, H. Giessen, *Nat. Photonics* **2009**, *3*, 157.
[4] D. Kim, J. Yu, I. Hwang, S. Park, F. Demmerle, G. Boehm, M.-C. Amann, M. A. Belkin, J. Lee, *Nano Lett.* **2020**, *20*, 8032.
[5] Y. Liu, X. Zhang, *Chem. Soc. Rev.* **2011**, *40*, 2494.
[6] D. A. B. Miller, *Science* **2023**, *379*, 41.
[7] C. Jung, G. Kim, M. Jeong, J. Jang, Z. Dong, T. Badloe, J. K. W. Yang, J. Rho, *Chem. Rev.* **2021**, *121*, 13013.
[8] B. Wang, F. Dong, H. Feng, D. Yang, Z. Song, L. Xu, W. Chu, Q. Gong, Y. Li, *ACS Photonics* **2018**, *5*, 1660.
[9] L. Cong, P. Pitchappa, Y. Wu, L. Ke, C. Lee, N. Singh, H. Yang, R. Singh, *Adv. Opt. Mater.* **2017**, *5*, 1600716.
[10] J. Zhou, H. Qian, C.-F. Chen, J. Zhao, G. Li, Q. Wu, H. Luo, S. Wen, Z. Liu, *Proc. Natl. Acad. Sci. USA* **2019**, *116*, 11137.
[11] H. Kwon, A. Cordaro, D. Sounas, A. Polman, A. Alù, *ACS Photonics* **2020**, *7*, 1799.
[12] G. Zheng, H. Mühlenbernd, M. Kenney, G. Li, T. Zentgraf, S. Zhang, *Nat. Nanotechnol.* **2015**, *10*, 308.
[13] Y. Wang, Q. Wang, Z. Li, X. Lan, W. Gao, Q. Han, J. Qi, J. Dong, *J. Phys. Chem. C* **2021**, *125*, 25243.
[14] B. Ai, H. M. Luong, Y. Zhao, *Nanoscale* **2020**, *12*, 2479.
[15] F. Wang, Z. Han, J. Sun, W. Ali, X. Wang, Z. Tang, *Nano Res.* **2023**. https://doi.org/10.1007/s12274-023-5518-0
[16] R. M. Kim, J.-H. Huh, S. Yoo, T. G. Kim, C. Kim, H. Kim, J. H. Han, N. H. Cho, Y.-C. Lim, S. W. Im, E. Im, J. R. Jeong, M. H. Lee, T.-Y. Yoon, H.-Y. Lee, Q.-H. Park, S. Lee, K. T. Nam, *Nature* **2022**, *612*, 470.
[17] J. Lv, D. Ding, X. Yang, K. Hou, X. Miao, D. Wang, B. Kou, L. Huang, Z. Tang, *Angew. Chem., Int. Ed.* **2019**, *58*, 7783.
[18] Y. Yang, H. Kim, T. Badloe, J. Rho, *Nanophotonics* **2022**, *11*, 4123.
[19] Z. Han, F. Wang, J. Sun, X. Wang, Z. Tang, *Adv. Mater.* **2023**, *35*, 2206141.
[20] Y. Xie, P. Yang, L. Deng, Z. Feng, J. Li, C. Zhang, X. Tang, C. Li, J. Li, L. Xu, D. Zhang, X. Chen, G. Zou, *Adv. Opt. Mater.* **2022**, *10*, 2102197.
[21] H. L. Liu, B. Zhang, T. Gao, X. Wu, F. Cui, W. Xu, *Nanoscale* **2019**, *11*, 5506.
[22] I. Kim, W.-S. Kim, K. Kim, M. A. Ansari, M. Q. Mehmood, T. Badloe, Y. Kim, J. Gwak, H. Lee, Y.-K. Kim, J. Rho, *Sci. Adv.* **2021**, *7*, eabe9943.
[23] H. S. Khaliq, J. Kim, T. Naeem, K. Riaz, T. Badloe, J. Seong, J. Akbar, M. Zubair, M. Q. Mehmood, Y. Massoud, J. Rho, *Adv. Opt. Mater.* **2022**, *10*, 2201175.

[24] C.-W. Lee, H. J. Choi, H. Jeong, *Nano Convergence* **2020**, *7*, 3.

[25] M. J. Schnermann, *Nature* **2017**, *551*, 176.

[26] Y. Chen, S. Wang, F. Zhang, *Nat. Rev. Bioeng.* **2023**, *1*, 60.

[27] S. Huang, C. Lin, J. Qi, A. M. Iyer, Y. He, Y. Li, N. M. Bardhan, D. J. Irvine, P. T. Hammond, A. M. Belcher, *Adv. Mater.* **2021**, *33*, 2006057.

[28] K. De Greve, L. Yu, P. L. McMahon, J. S. Pelc, C. M. Natarajan, N. Y. Kim, E. Abe, S. Maier, C. Schneider, M. Kamp, S. Höfling, R. H. Hadfield, A. Forchel, M. M. Fejer, Y. Yamamoto, *Nature* **2012**, *491*, 421.

[29] E. N. Economou, *Phys. Rev.* **1969**, *182*, 539.

[30] Z. Wu, X. Chen, M. Wang, J. Dong, Y. Zheng, *ACS Nano* **2018**, *12*, 5030.

[31] R. Ortuño, C. García-Meca, F. J. Rodríguez-Fortuño, J. Martí, A. Martínez, *Phys. Rev. B* **2009**, *79*, 075425.

[32] K. H. Park, J. Kwon, U. Jeong, J.-Y. Kim, N. A. Kotov, J. Yeom, *ACS Nano* **2021**, *15*, 15229.

[33] L. Hu, H. Dai, F. Xi, Y. Tang, F. Cheng, *Opt. Commun.* **2020**, *473*, 125947.

[34] P. T. Probst, M. Mayer, V. Gupta, A. M. Steiner, Z. Zhou, G. K. Auernhammer, T. A. F. König, A. Fery, *Nat. Mater.* **2021**, *20*, 1024.

[35] J. Lv, K. Hou, D. Ding, D. Wang, B. Han, X. Gao, M. Zhao, L. Shi, J. Guo, Y. Zheng, X. Zhang, C. Lu, L. Huang, W. Huang, Z. Tang, *Angew. Chem., Int. Ed.* **2017**, *56*, 5055.

[36] M. Cen, J. Wang, J. Liu, H. He, K. Li, W. Cai, T. Cao, Y. J. Liu, *Adv. Mater.* **2022**, *34*, 2203956.

[37] T. Gissibl, S. Thiele, A. Herkommer, H. Giessen, *Nat. Commun.* **2016**, *7*, 11763.

[38] S. Takahashi, T. Tajiri, Y. Ota, J. Tatebayashi, S. Iwamoto, Y. Arakawa, *Appl. Phys. Lett.* **2014**, *105*, 051107.

[39] Z. Liu, Y. Xu, C. Ji, S. Chen, X. Li, X. Zhang, Y. Yao, J. Li, *Adv. Mater.* **2020**, *32*, 1907077.

[40] W. Wu, Y. Battie, V. Lemaire, G. Decher, M. Pauly, *Nano Lett.* **2021**, *21*, 8298.

[41] Y. Tang, Z. Liu, J. Deng, K. Li, J. Li, G. Li, *Laser Photonics Rev.* **2020**, *14*, 2000085.

[42] C. Wang, Z. Li, R. Pan, W. Liu, H. Cheng, J. Li, W. Zhou, J. Tian, S. Chen, *ACS Photonics* **2020**, *7*, 3415.

[43] T. Cao, Y. Li, C.-W. Wei, Y. Qiu, *Opt. Express* **2017**, *25*, 9911.

[44] A. Basiri, X. Chen, J. Bai, P. Amrollahi, J. Carpenter, Z. Holman, C. Wang, Y. Yao, *Light: Sci. Appl.* **2019**, *8*, 78.

[45] B. Lyu, Y. Li, Q. Jia, H. Li, G. Yang, F. Cao, S. Kou, D. Liu, T. Cao, G. Li, J. Shi, *Laser Photonics Rev.* **2023**, *17*, 2201004.

[46] B. M. Maoz, A. B. Moshe, D. Vestler, O. Bar-Elli, G. Markovich, *Nano Lett.* **2012**, *12*, 2357.

[47] P. Lai, G. Dong, W. Wang, T. Chen, T. Lv, B. Lv, Z. Zhu, Y. Li, C. Guan, J. Shi, *Opt. Express* **2020**, *28*, 15071.

[48] S. Zanotto, G. Mazzamuto, F. Riboli, G. Biasiol, G. C. La Rocca, A. Tredicucci, A. Pitanti, *Nanophotonics* **2019**, *8*, 2291.

[49] Z. Wu, Y. Zheng, *Adv. Opt. Mater.* **2017**, *5*, 1700034.

[50] M. Nishida, N. Hatakenaka, Y. Kadoya, *Phys. Rev. B* **2015**, *91*, 235406.

[51] Y. Tang, A. E. Cohen, *Phys. Rev. Lett.* **2010**, *104*, 163901.

[52] S. W. D. Lim, M. L. Meretska, F. Capasso, *Nano Lett.* **2021**, *21*, 8642.

[53] V. Sajeev, A. Jana, S. Mallick, K. M. Devi, D. R. Chowdhury, *J. Phys. Photonics* **2022**, *4*, 045001.

[54] T.-H. Park, N. Mirin, J. B. Lassiter, C. L. Nehl, N. J. Halas, P. Nordlander, *ACS Nano* **2008**, *2*, 25.

[55] W. Li, Z. J. Coppens, L. V. Besteiro, W. Wang, A. O. Govorov, J. Valentine, *Nat. Commun.* **2015**, *6*, 8379.

[56] A. Li, X. Wang, L. Guo, S. Li, *J. Phys. Chem. C* **2019**, *123*, 25394.

[57] J. Henzie, M. H. Lee, T. W. Odom, *Nat. Nanotechnol.* **2007**, *2*, 549.

[58] A. Attiaoui, G. Daligou, S. Assali, O. Skibitzki, T. Schroeder, O. Moutanabbir, *Adv. Mater.* **2023**, *35*, 2300595.

[59] S. Both, M. Schäferling, F. Sterl, E. A. Muljarov, H. Giessen, T. Weiss, *ACS Nano* **2022**, *16*, 2822.

[60] J. García-Guirado, M. Svedendahl, J. Puigdollers, R. Quidant, *Nano Lett.* **2020**, *20*, 585.

[61] COMSOL Multiphysics v. 6.1. www.comsol.com, COMSOL AB, Stockholm, Sweden.

[62] P. B. Johnson, R. W. Christy, *Phys. Rev. B* **1972**, *6*, 4370.